The evolving far-IR galaxy luminosity function and dust-obscured star-formation rate density out to $z \simeq 5$

M. P. Koprowski, J. S. Dunlop, M. J. Micha lowski, K. E. K. Coppin, J. E. Geach, R. J. McLure, D. Scott and P. P. van der Werf

We present a new measurement of the evolving galaxy far-IR luminosity function (LF) extending out to redshifts $z \simeq 5$, with resulting implications for the level of dust-obscured star-formation density in the young Universe. To achieve this we have exploited recent advances in sub-mm/mm imaging with SCUBA-2 on the James Clerk Maxwell Telescope (JCMT) and the Atacama Large Millimeter/Submillimeter Array (ALMA), which together provide unconfused imaging with sufficient dynamic range to provide meaningful coverage of the luminosity-redshift plane out to $z > 4$. Our results support previous indications that the faint-end slope of the far-IR LF is sufficiently flat that comoving luminosity-density is dominated by bright objects ($\simeq L^*$). However, we find that the number-density/luminosity of such sources at high redshifts has been severely over-estimated by studies that have attempted to push the highly-confused Herschel SPIRE surveys beyond $z \simeq 2$. Consequently we confirm recent reports that cosmic star-formation density is dominated by UV-visible star formation at $z > 4$. Us- ing both direct ($1/V_{\rm max}$) and maximum likelihood determinations of the LF, we find that its high-redshift evolution is well characterized by continued positive luminosity evolution coupled with negative density evolution (with increasing redshift). This explains why bright sub-mm sources continue to be found at $z > 5$, even though their integrated contribution to cosmic star-formation density at such early times is very small. The evolution of the far-IR galaxy LF thus appears similar in form to that already established for active galactic nuclei, possibly reflecting a similar dependence on the growth of galaxy mass.

DATA

We used the data collected as a part of the SCUBA-2 Cosmology Legacy Survey (S2CLS; Geach et al. 2017). The fields utilised here are the UKIDSS- UDS, where the 850-μm imaging covers $\simeq 0.9$ deg^2 with a 1σ noise of 0.9 mJy (revealing 1085 sources with a signal-to-noise ratio SNR > 3.5), and the COSMOS field, where the 850-μm imaging covers $\simeq 1.3$ deg^2 with the 1σ noise of 1.6 mJy (revealing 719 sources with SNR > 3.5). To help inform the measurement of the faint-end slope of the LF, we used the ALMA 1.3-mm imaging of the HUDF undertaken by Dunlop et al. (2017). A mosaic of 45 ALMA pointings was created to cover the full $\simeq 4.5$ arcmin^2 area previously imaged with WFC3/IR on HST. The ALMA map reached a noise level of $\sigma_{1.3} \simeq 35$ μJy beam^{-1} , and 16 sources were detected with flux densities $S_{1.3} >$ 120 μJy. In addition, various ancillary data from UV to radio was utilised.

REDSHIFTS

Because of the beam size of the JCMT SCUBA-2 imaging at 850 μm (FWHM ≃ 15 arcsec), to identify optical/near-IR counterparts, we used the method outlined in Downes et al. (1986), where we adopt a 2.5σ search radius around the SCUBA-2 position based on the signal-to-noise ratio (SNR): $r_{\rm S} = 2.5 \times 0.6 \times$ FWHM/SNR. Within this radius we calculated the corrected Poisson probability, p, that a given counterpart could have been selected by chance. Three imaging wavebands were used when searching for galaxy counterparts: the VLA 1.4-GHz imaging, the Spitzer MIPS 24-μm imaging, and the Spitzer IRAC 8-μm imaging. Once the counterparts were found in each of these bands, they were matched with the optical/near-IR catalogues using a search radius of $r = 1.5$ arcsec and the closest object taken to be the galaxy counterpart. We used the available multi-wavelength data to derive the optical/near-IR photometric redshifts with a code based on the HYPERZ package (Bolzonella et al. 2000), with the stellar population synthesis models of Bruzual & Charlot (2003), with the Chabrier (2003) stellar initial mass function (IMF), with Calzetti et al. (2000) dust attenuation law. The final redshift distributions are shown in Figure 1.

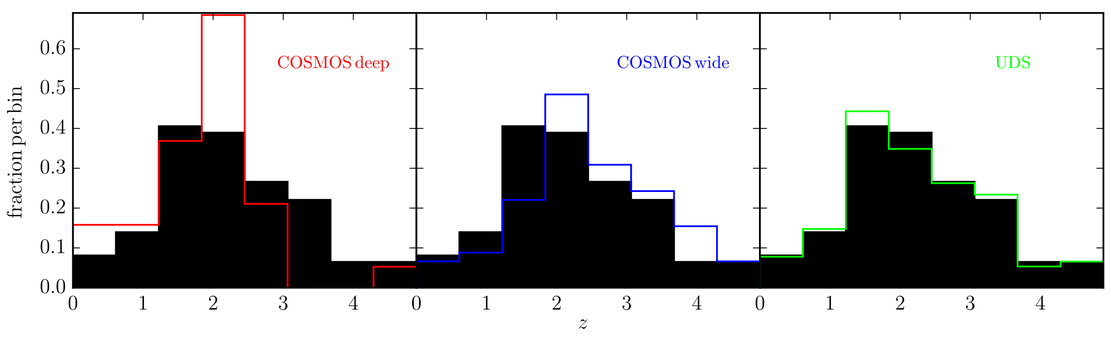

FIGURE 1. The redshift distributions of the refined SCUBA-2 source samples used in this work. The black histogram depicts the distribution for all the sources, and yields a mean redshift of $z = 2.73 \pm 0.06$. From the top, the colour plots show the COSMOS deep, COSMOS wide and the UDS redshift distributions with $z = 2.30 \pm 0.23$, $z = 3.05 \pm 0.17$ and $z = 2.70 \pm 0.07$ respectively

IR LFS

To derive the evolving far-IR LF, $\Phi_{\rm IR}$, we use two independent methods. One is the standard $1/V_{\rm max}$ method (Schmidt 1968), where we then fit a set of Schechter functions. In order to find the continuous form of the redshift evolution of the far- IR LF, we additionally use the maximum-likelihood (ML) method presented in Marshall et al. (1983).

For 1/Vmax method, the LF in a given luminosity and redshift bin is calculated using:

$$\Phi(L,z) = \frac{1}{\Delta L} \sum_i \frac{1-{\rm FDR}}{w_i \times V_{{\rm max},i}},$$

where ΔL is the width of the luminosity bin, FDR is the false detection rate, $w_{\rm i}$ is the completeness for the i-th galaxy and $V_{\rm max,i}$ is the co-moving volume available to the i-th source. For S2CLS sources the false detection rate is (from Geach et al. 2017):

$$\log_{10}({\rm FDR}) = 2.67 - 0.97 \times {\rm SNR}.$$

The available co-moving volume is:

$$V_{{\rm max},i} = \sum_j \frac{\Omega_j}{4\pi} V_{{\rm max},j},$$

where we sum over all the available S2CLS fields and Ωj is the solid angle subtended by the j-th field on the sky.

The likelihood function used here (Marshall et al. 1983) is defined as a product of the probabilities of observing exactly one source in $dzdL$ at the position of the i-th galaxy (zi,Li) for N galaxies in our sample and of the probabilities of ob- serving zero sources in all the other differential elements in the luminosity-redshift plane. Using Poisson probabilities, the likelihood is:

$$\mathscr{L} = \prod_i^N \lambda_i e^{-\lambda_i} \prod_j e^{-\lambda_j},$$

where j runs over all differential elements in which no sources were observed, and λ is the expected number of galaxies in $dzdL$ at z,L:

$$\lambda = \Phi(z,L)\Omega(z,L)\frac{dV}{dz}dzdL,$$

with Ω being the fractional area of the sky in which a galaxy with a given z and L can be detected in our fields.

The resulting $1/V_{\rm max}$ IR LFs are shown in Figure 2 in colour with the corresponding ML curves in black.

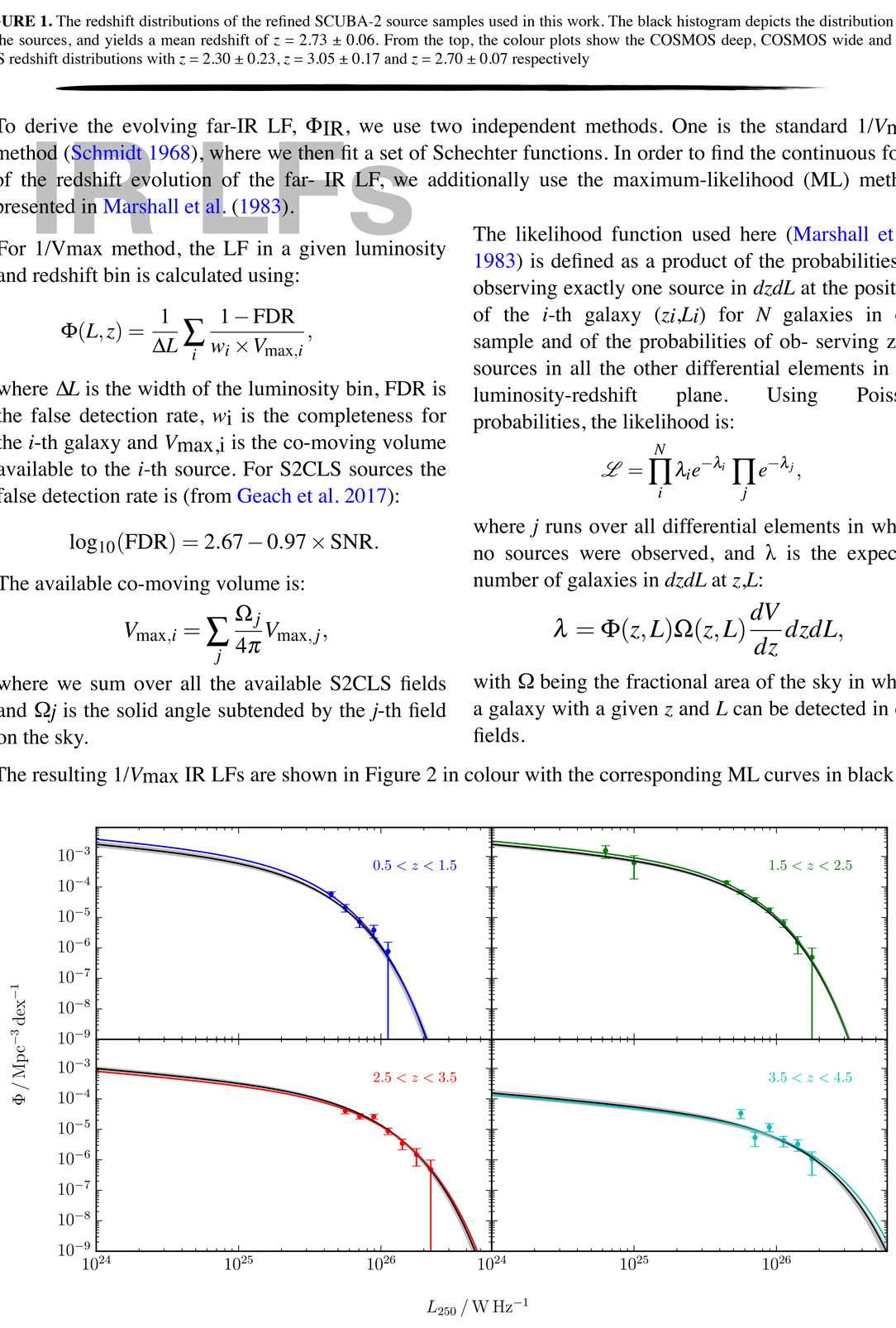

FIGURE 2. The far-IR (rest-frame 250-μm) galaxy luminosity functions (LFs) for the four redshift bins studied in this work. The points with error bars show the LF values determined using the $1/V_{\rm max}$ method. The two faintest points in the $1.5 < z < 2.5$ redshift bin depict the LF values found using the ALMA data. These allowed us to determine the faint-end slope $\alpha = -0.4$, which was then adopted for the other redshift bins. The coloured solid lines show the best-fitting Schechter functions to these data points. The black solid lines (almost perfectly aligned with the coloured solid lines) depict the results of the maximum-likelihood method, with the derived uncertainty indicated by the shaded grey region.

SFRD

Having constructed the rest-frame 250-μm LFs, it is now possible to establish the redshift evolution of the star formation rate density (SFRD). We first integrate the LFs weighted by the total IR luminosity (8–1000μm), where the LFs were integrated down to a lower luminosity limit of $0.01 \times L^*$. The resulting inferred total IR luminosity density was then converted into dust-obscured star-formation rate density at each redshift using the scaling factor of Kennicutt (1998), with an additional multiplicative factor of 0.63 to convert from a Salpeter to a Chabrier IMF. The results are shown in Figure 3. The red filled squares depict the values of SFRD derived from the four LFs shown in Figure 2, established using the $1/V_{\rm max}$ method. The red solid line shows the evolution of SFRD as determined from the continuous form of the redshift evolution of the LF found using the maximum-likelihood method, with the grey area showing the 1σ errors. The blue squares give the values of UV-visible SFRD derived from the Parsa et al. (2016), while the black solid line shows the total SFRD calculated by simply adding the IR and UV estimates. The black dotted and dashed lines depict the alternative functional forms of the redshift evolution of total SFRD provided by Madau & Dickinson (2014) and Behroozi et al. (2013) respectively (after conversion to a Chabrier IMF).

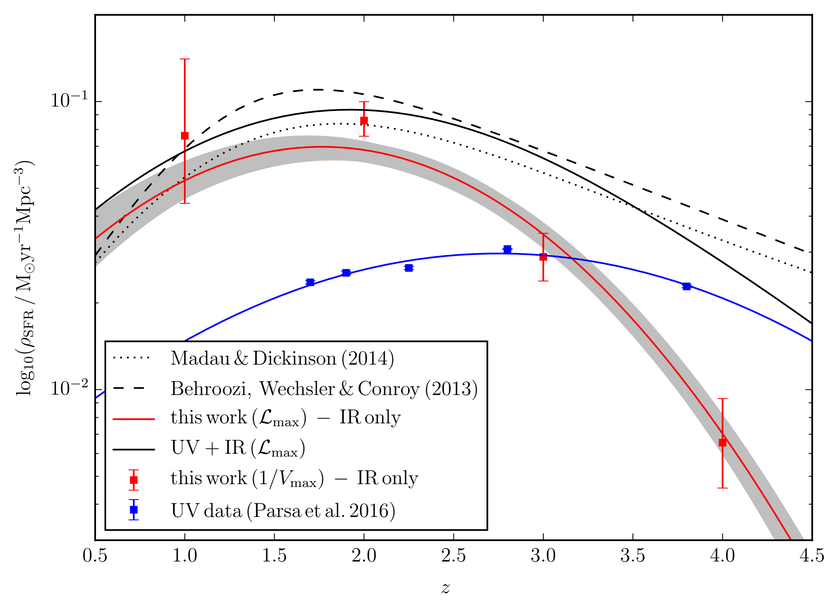

FIGURE 3. The star formation rate density as a function of redshift. See above text for details.

EVOLUTION

Finally, we discuss how the form of the LF evolution uncovered here naturally explains the apparent 'down-sizing' of the sub-mm source population. In the left panel of Figure 4 we plot our evolving LFs as a function of redshift from $z \simeq 0.5$ to $z \simeq 4.5$. At low redshifts, the increase in both Φ* and L* produces an increase in both the number density of sources, and luminosity density with increasing redshift. At high redshifts the decline in Φ* progressively overcomes the continued positive evolution of L* to produce a decline in both these quantities, but it can be seen that the continued positive evolution of L* means that the most luminous sources persist, or indeed are preferentially found at the highest redshifts explored here.

To better connect with observables, we have used our evolving LF to calculate the predicted redshift distribution of 850-μm sources as a function of flux density. The results are shown for four different flux-density thresholds in the right panel of Figure 4. Here it can be seen that the peak in the redshift distribution is expected to naturally increase gradually from $z \simeq 1.8$ for $S850 > 1$mJy to $z \simeq 3$ for $S850 > 10$mJy. This is in excellent accord with what has been reported in the literature (e.g. Koprowski et al. 2014; Michałowski et al. 2016) and clarifies why, although dust-enshrouded star-formation is globally less important than UV-visible star-formation activity at $z > 4$, bright sub-mm sources will continue to be discovered out to high redshifts.

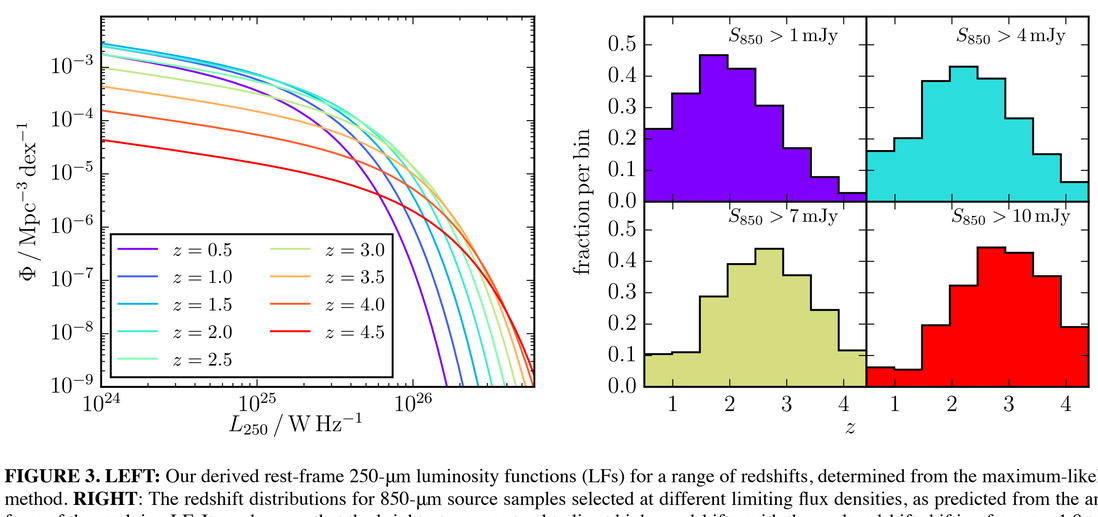

FIGURE 3. LEFT: Our derived rest-frame 250-μm luminosity functions (LFs) for a range of redshifts, determined from the maximum-likelihood method. **RIGHT**: The redshift distributions for 850-μm source samples selected at different limiting flux densities, as predicted from the analytic form of the evolving LF. It can be seen that the brightest sources tend to lie at higher redshifts, with the peak redshift shifting from $z \simeq 1.8$ to $z \simeq 3$ over the flux-density range explored here.

SUMMARY

We have analysed the coverage of the far-IR luminosity–redshift plane provided by (sub-)mm-selected galaxy samples extracted from the S2CLS and ALMA imaging of the HUDF to make a new measurement of the evolving galaxy far-IR luminosity function (LF) extending out to redshifts $z \simeq 5$. Using both direct ($1/V$max) and maximum-likelihood methods we have determined the form and evolution of the rest-frame 250-μm galaxy LF. This LF is well described by a Schechter function with a faint-end slope $\alpha \simeq -0.4$ (derived using the ALMA data at $z \simeq 2$) which displays a combination of rising-then- falling density evolution, and positive luminosity evolution.

We have utilised our measurement of the evolving IR LF to derive comoving IR luminosity density, and hence obscured SFRD, which we then combine with UV-estimates of unobscured activity (from Parsa et al. 2016), to derive the evolution of total SFRD. Consistent with several other recent studies (e.g. Bourne et al. 2017; Dunlop et al. 2017; Liu et al. 2017) we find that SFRD declines beyond $z \simeq 2 - 2.5$ and is dominated by UV-visible star-formation activity beyond $z \simeq 4$.

Finally, we show how the evolution of the IR LF as derived here (with its combination of rising-then-falling characteristic density (Φ*), and positive evolution of characteristic luminosity density (L*)) with redshift, produces a decline in inferred SFRD beyond $z \simeq 2 - 2.5$ while at the same time predicting that the most luminous sub-mm sources will continue to be found out to very high redshifts ($z \simeq 5 - 6$). Specifically, our evolving LF, with its combined luminosity+density evolution, predicts that the median redshift of sub-mm sources should increase with increasing flux density, consistent with several reports in the recent literature.

— Behroozi P. S., Wechsler R. H., Conroy C., 2013, ApJ, 770, 57 — Bolzonella M., Miralles J.-M., Pell´o R., 2000, A&A, 363, 476 — Bourne N., et al., 2017, MNRAS, 467, 1360 — Bruzual G., Charlot S., 2003, MNRAS, 344, 1000 — Calzetti D., Armus L., Bohlin R. C., Kinney A. L., Koornneef J., Storchi-Bergmann T., 2000, ApJ, 533, 682 — Chabrier G., 2003, ApJ, 586, L133 — Dunlop J. S., et al., 2017, MNRAS, 466, 861 — Geach J. E., et al., 2017, MNRAS, 465, 1789 — Kennicutt Jr. R. C., 1998, ARA&A, 36, 189 — Koprowski M. P., Dunlop J. S., Micha lowski M. J., Cirasuolo M., Bowler R. A. A., 2014, MNRAS, 444, 117 — Liu D., et al., 2017, preprint, (arXiv:1703.05281) — Madau P., Dickinson M., 2014, ARA&A, 52, 415 — Marshall H. L., Tananbaum H., Avni Y., Zamorani G., 1983, ApJ, 269, 35 — Micha lowski M. J., et al., 2016, preprint, (arXiv:1610.02409) — Parsa S., Dunlop J. S., McLure R. J., Mortlock A., 2016, MNRAS, 456, 3194 — Schmidt M., 1968, ApJ, 151, 393